buildings

MDPI

Article

Bearing Capacity of UHPC-Filled High-Strength Elliptical Steel Tube Composite Columns with Encased High-Strength H-Shape Steel Subjected to Eccentrical Load

Jing Ji [1,2,3], Weichen Wang [2], Liangqin Jiang [2], Hongguo Ren [4,*], Qingqin Wang [5], Wenyu Xuan [4,*] and Yingchun Liu [2]

1 China-Pakistan Belt and Road Joint Laboratory on Smart Disaster Prevention of Major Infrastructures, Southeast University, Nanjing 211189, China
2 Heilongjiang Key Laboratory of Disaster Prevention, Mitigation and Protection Engineering, Northeast Petroleum University, Daqing 163319, China
3 Jiangsu Southeast Special Engineering & Technology Co., Ltd., Nanjing 210000, China
4 Handan Key Laboratory of Building Physical Environment and Regional Building Protection Technology, School of Architecture and Art, Hebei University of Engineering, Handan 056038, China
5 China Academy of Building Research Co., Ltd., Beijing 100029, China
* Correspondence: renhongguo771126@163.com (H.R.); xuanwenyuhbgcxy@163.com (W.X.)

Abstract: In order to investigate the bearing capacity of composite columns composed of ultra-high performance concrete, (UHPC)-filled high-strength elliptical steel tube with encased high-strength H-shape steel (HUCFESTCs) were subjected to eccentric load. Forty-four HUCFESTCs were designed with varying parameters: yield strength of the steel tube (f_y), yield strength of the H-shape steel (f_{y1}), concrete-cube compressive strength (f_{cu}), steel tube thickness (t), eccentricity (e), slenderness ratio (λ), the section area of the H-shape steel (A_{HS}), and long–short axis ratio (ψ). Based on a bilinear elastic–plastic constitutive model of steel that considered stress hardening and a nonlinear constitutive model of UHPC, 44 HUCFESTCs models were established by ABAQUS software. The influence of different parameters on the ultimate bearing capacity of the HUCFESTCs was analyzed. The whole process of HUCFESTCs under eccentric load was studied, and the typical failure modes of HUCFESTCs are described. The results show that the main failure mode of the HUCFESTCs subjected to eccentrical load is bulging outward of the steel tube, the buckling of the H-shape steel, and crushing of the concrete in the middle part of the column and the inner part of the H-shape steel. The stiffness of HUCFESTCs increases gradually with the increase in f_y, t, and e. The ultimate eccentrical compression bearing capacity of HUCFESTCs improves gradually with increases in f_y, t, f_{y1}, A_{HS}, ψ, and f_{cu}, but it decreases gradually with increases in λ and e. By using statistical regression and introducing the reduction coefficient of eccentricity, the calculation formula for the eccentric bearing capacity of HUCFEST columns is developed, which can provide a basis for the application of HUCFESTCs in practical engineering.

Keywords: high-strength elliptical steel tube; high-strength H-shape steel; UHPC; eccentrical load; bearing capacity

Citation: Ji, J.; Wang, W.; Jiang, L.; Ren, H.; Wang, Q.; Xuan, W.; Liu, Y. Bearing Capacity of UHPC-Filled High-Strength Elliptical Steel Tube Composite Columns with Encased High-Strength H-Shape Steel Subjected to Eccentrical Load. *Buildings* **2022**, *12*, 1272. https://doi.org/10.3390/buildings12081272

Academic Editor: Jia-Bao Yan

Received: 8 July 2022
Accepted: 15 August 2022
Published: 19 August 2022

1. Introduction

The study of composite columns composed of concrete-filled elliptical steel tube (CFESTCs) has recently attracted much interest internationally. CFESTCs not only have the advantages of high bearing capacity and excellent ductility, but also can provide favorable strong and weak axes for the structure owing to their special section form [1,2]. At the same time, with the continuous development of building materials, ultrahigh performance concrete (UHPC) had been widely used owing to its ultrahigh strength and excellent durability [3–5]. As concrete materials usually have characteristics of high brittleness,

increasing the bearing capacity [6] and flexural rigidity [7] by adding steel sections into composite columns of concrete-filled steel tubes is essential.

Considering the special cross-sectional form of the CFESTCs, many scholars have carried out a large number of experiments on the mechanical properties of CFESTCs in recent years. In 2012, Sheehan et al. [8] conducted tests on eight CFESTCs under eccentrical load. Based on the test data, extended parameter analysis was carried out by using ABAQUS finite element (FE) simulation software. The results showed that yield strength of steel tube (f_y), strength of concrete (f_c), thickness of steel tube (t), and ratio of the long-stub axis (ψ) had an obvious influence on the ultimate bearing capacity (N_{um}) of CFESTCs subjected to eccentric load. With increasing f_y, f_c, and t, N_{um} of CFESTCs gradually increased, while N_{um} of CFESTCs gradually decreased with increasing ψ. In 2017, tests on eight CFESTCs under eccentrical and axial load were conducted by Yang et al. [9]. The constitutive model for CFESTCs was established. The test results showed that N_{um} of CFESTCs decreased gradually with increasing slenderness ratio (λ) and eccentricity (e). The design method of CFESTCs given in the Code for the Design of Concrete-Filled Steel Tube Structures (GB50936) and the design method of CFSTCs in the European Code for Reinforced Concrete (EC4) could be applied to CFESTCs with a height–width ratio between 1.0 and 2.5. On the basis of these previous experiments, the researchers began to carry out detailed finite element analysis of the CFESTCs [10]. In 2021, FE simulation on composite stub columns composed of a concrete-filled double steel tube with an elliptical hollow section (CFEDSTCs) was conducted by Ipek et al. [11]. The results indicated that with an increase in f_y and f_c, the axial bearing capacity of CFEDSTCs gradually increased. Additionally, there was no significant influence on the initial stiffness of the composite columns by the increase in f_y and f_c. The research described above showed that the change law of mechanical properties of elliptical CFST composite columns under the action of axial and eccentric loads was similar to that of ordinary CFST.

Simultaneously, with the continuous improvement in architectural design standards, the strength requirements of buildings for composite structures have also increased. Therefore, ultrahigh performance concrete has begun to be widely used in composite structures. On this basis, the UHPC-filled steel tube composite columns (UCFSTCs) began to be widely studied. In 2013, Guler et al. [12] conducted tests on UCFSTCs. The results indicated that increasing the thickness of the steel tube could significantly enhance the structural ductility after peak load, thus reducing the structural risk caused by the high brittleness of UHPC. From 2020 to 2021, Wei et al. [13,14] conducted tests on 21 composite columns composed of UHPC-filled high-strength steel tube (UCFHSTCs) under an axial load. Furthermore, the results showed that when compared with UCFSTCs, the high-strength steel tube of UCFHSTCs could better restrain UHPC. The main failure mode of the steel tubes was local buckling, and the main failure mode of the concrete was shear failure. Numerous studies have shown that UHPC without fiber reinforcement has poor ductility. Therefore, higher strength steel tubes were required to improve the ductility of the UCFSTCs.

Since there was rarely an optimum axial load in engineering practice, CFSTCs are frequently under stress from eccentric loads. Therefore, it was particularly important to study the CFSTCs subjected to an eccentric load. Research on composite columns composed of GFRP pipe–concrete–steel tube under eccentrical load and H-shaped honeycombed steel web composite columns with a rectangular concrete-filled steel tube subjected to eccentrical load were carried out by Ji et al. [15,16] in 2021 and 2022, respectively, and the results revealed that as the steel-tube yield strength increased, the bearing capacity to eccentric compression gradually increased, but as eccentricity increased, the N_{um} of specimens declined gradually. In 2019, Ma et al. [17] conducted tests on 17 recycled composite columns composed of concrete-filled steel tube with section steel (RACFSTCs) subjected to eccentric compression load. The results showed that the main failure modes of the RACFSTCs were buckling of the steel tube and material damage of the concrete. The composite columns showed good ductility and deformation capacity under eccentric load. At the same time, with an increase in steel tube yield strength and section steel yield strength, the bearing

capacity to eccentric compression gradually increased. These research results show that the ductility of the composite column can be effectively improved by increasing the steel content and placing the section steel in the composite columns.

Currently, research on concrete-filled elliptical steel tube composite columns mainly focuses on the axial compression performance [18–20] of concrete-filled elliptical steel tube composite stub columns and the eccentric compression performance of long columns [21]. However, comparatively few studies have been conducted on the compression performance of composite columns composed of UHPC-filled elliptical steel tube subjected to eccentric load. Considering that the ductility of UHPC without fiber reinforcement was lower than that of conventional concrete [22,23], this paper proposes a novel type of the composite columns composed of UHPC-filled high-strength elliptical steel tube with encased high-strength H-shape steel (HUCFESTCs). Based on a bilinear elastic–plastic constitutive model of steel that considers stress hardening and applies a nonlinear constitutive model of UHPC, ABAQUS software was used to investigate the mechanical behavior of HUCFESTCs with varying parameters. Statistical regression was used to suggest a formula for the bearing capacity of HUCFESTCs subjected to eccentrical load.

2. Specimen Design

In order to investigate the bearing capacity of HUCFESTCs subjected to eccentric load, 44 HUCFESTCs were designed, and the main parameters were steel tube strength f_y (from 500 to 700 MPa), yield strength f_{y1} of H-shape steel (from 500 to 700 MPa), cube compressive strength of concrete f_{cu} (from 100 to 135 MPa), thickness of steel tube t (from 2 to 8 mm), eccentricity e (from 30 to 70 mm), slenderness ratio λ (from 2 to 3), section area of H-shape steel A_{HS} (from 680 to 1180 mm^2), and long–short axis ratio ψ (from 1 to 2). The schematic diagram of the HUCFESTC cross-section is shown in Figure 1; a is the radius of the long axle, b is the radius of the stub axle, t is the thickness of the steel tube, h_1 is the width of the web plate of the H-shape steel, h_2 is the flange width of the H-shape steel, t_1 is the flange thickness of the H-shape steel, and t_2 is the web plate thickness of the H-shape steel. The H-shape steel in this paper includes, in mm: H_1 (t_1 = 6.5, t_2 = 4, h_1 = 100, h_2 = 60), H_2 (t_1 = 5, t_2 = 4, h_1 = 100, h_2 = 60), and H_3 (t_1 = 4, t_2 = 2, h_1 = 100, h_2 = 60).

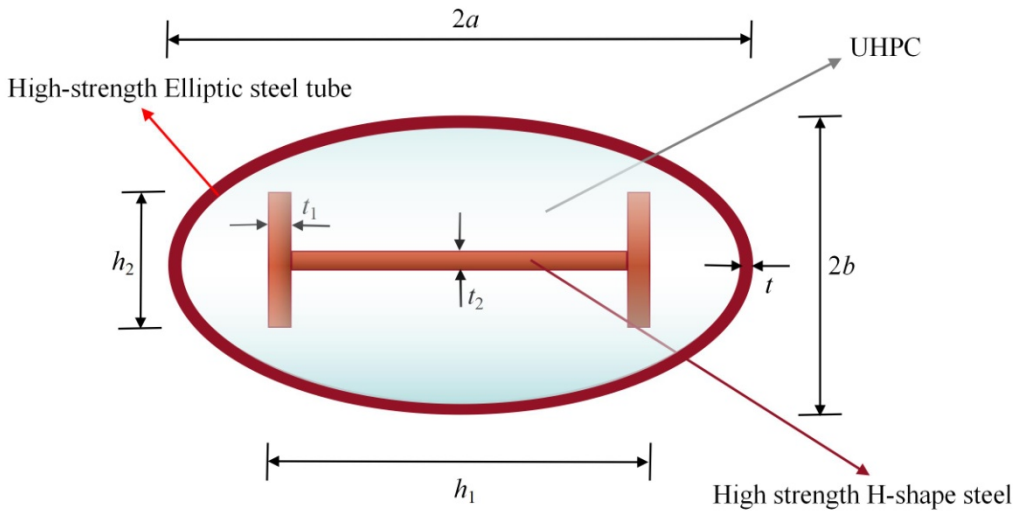

Figure 1. Schematic diagram of the HUCFESTC cross-section. a is the radius of the long axle, b is the radius of the stub axle, t is the thickness of the steel tube, h_1 is the width of the web plate of the H-shape steel, h_2 is the flange width of the H-shape steel, t_1 is the flange thickness of the H-shape steel, and t_2 is the web plate thickness of the H-shape steel.

3. FE Model

3.1. Constitutive Model for Materials

3.1.1. Steel

In this paper, both high-strength steel tubes and high-strength H-shape steels adopt the double-line elastic–plastic constitutive model considering stress hardening. The steel tension and compression strain relationship is shown in Equation (1); ε_y and f_y are the yield strain and yield strength of steel, respectively. E_s is equal to 0.1 E in Equation (1). Moreover, the elastic modulus (E_s) of the steel is 2.06 × 10^5 MPa and Poisson's ratio of the steel is 0.3.

$$\sigma = \begin{cases} E \times \varepsilon & (\varepsilon \le \varepsilon_y) \\ f_y + E_s \times (\varepsilon - \varepsilon_y) & (\varepsilon > \varepsilon_y) \end{cases} \quad (1)$$

3.1.2. Material Modeling of Concrete

References [24–28] provide the constitutive models of concrete that take the effect of restraint into account. Currently, Wei et al. [12] have established that the strain hardening/softening rule of concrete confined by steel tubes put forth by Tao et al. [24] is appropriate for UHPC. Therefore, in this paper, the concrete constitutive model proposed by Tao et al. [24] is adopted, and on this basis, the influence coefficient of the long-stub axial ratio of elliptical steel tube (ω) is introduced. The concrete tension and compression strain relationship are shown in Equations (2) and (3).

The uniaxial stress(σ)–strain(ε) relationship of concrete confined by steel tubes follows:

$$\frac{\sigma}{f_c} = \begin{cases} \frac{(ax+bx^2)f_c}{1+(a-2)x+(b-1)x^2} & 0 < x \le 1 \\ f_r + (f_c - f_r)\exp\left[-\left(\frac{\varepsilon - \varepsilon_{cc}}{\omega\alpha}\right)^{\beta}\right]^2 & \varepsilon > \varepsilon_{cc} \end{cases} \quad (2)$$

where $x = \varepsilon/\varepsilon_{c0}$, $c = \frac{E_c\varepsilon_{c0}}{f_c}$, $d = \frac{(A-1)^2}{0.55} - 1$, $\varepsilon_0 = 0.00076 + \left[(0.626f_c - 4.33) \times 10^{-7}\right]^{0.5}$, $\omega = (a/b)^2$ $\varepsilon_{cc} = \varepsilon_0 \times E^{(k)}$, and $k = (2.9224 + 0.0036f_c)\left(\frac{f_b}{f_c}\right)^{0.3124 + 0.02f_c}$; f_c is the cylinder compressive strength of concrete, and other parameters refer to the literature [24].

In this paper, the failure energy criterion of concrete is adopted to consider the tensile softening performance:

$$G_F = (0.049d_{max}^2 - 0.5d_{max} + 26) \times \left(\frac{f_c}{10}\right)^{0.7} \text{N/m} \quad (3)$$

where d_{max} = 20 mm.

The elastic modulus of concrete is 4700 × $(f_c)^{0.5}$ MPa [29].

3.2. Contact Definition

Normal hard contact and tangential relative slip were assumed between steel tube and concrete along with H-shape steel and concrete, and the friction coefficient μ was selected as 0.6. In the normal direction, hard contact under pressure interference is adopted to force the steel tube's inner wall to contact the concrete's outer wall completely [30].

3.3. Establishment of the Finite Element Model and Determination of Boundary Conditions

Figure 2 presents the models created by ABAQUS software for the 44 HUCFESTCs. The eight-joint hexahedral element type (C3 D8 R) was adopted to simulate the steel tube, H-shape steel, and concrete. Two reference points, designated RP-1 and RP-2, were placed close to the upper and bottom surfaces of the columns. In turn, the top and bottom of the columns were connected to the reference points. RP-1 imposed restrictions on the displacements (U_x, U_y, UR_x, UR_z) of the top end for columns, and RP-2 imposed restrictions on the displacements (U_x, U_y, U_z, UR_x, UR_z) of the bottom end for columns.

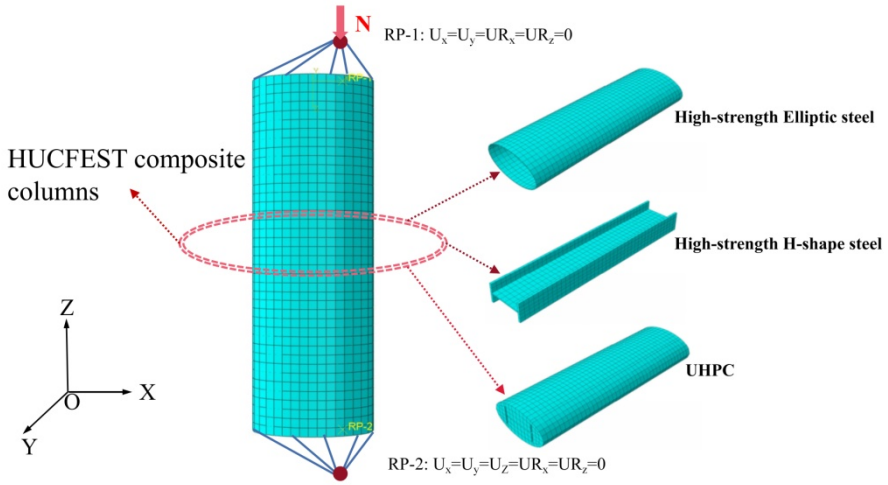

Figure 2. The FE models for the 44 HUCFESTCs.

4. Comparison of Test Curves and Simulation Curves

In order to verify the boundary conditions of the finite element model and the constitutive model, 18 specimens were selected from the literature [9,12,19,31,32]. Figure 3 displays the vertical load–displacement curves of 18 specimens. It is clear from Figure 3 that the test curves and the FE simulation curves are largely consistent. The parameters of 18 specimens are displayed in Table 1. Figure 4 and Table 1 compare the simulated bearing capacity (N_a) and the experimental bearing capacity (N_t), and it is clear that there is a maximum error of 5.5% between them, which can meet the requirements for engineering precision. As a result, using the FE modeling approach provided, it was feasible to replicate the eccentrical compression behavior of HUCFESTCs.

Table 1. The comparison between N_a and N_t.

Specimens		*a*/*b*	*t*/mm	f_y/MPa	f_{y1}/MPa	f_{ck}/MPa	*e*/mm	N_a/kN	N_t/kN	$\left\|\frac{N_a-N_t}{N_t}\right\|\times100\%$
Wei et al. [13]	UCS-1	1	4.4	1020	0	142.1	0	4536.15	4436.23	2.25
	UCS-2	1	6.2	1153	0	142.1	0	5482.38	5693.65	3.71
	UCS-3	1	10.4	773	0	142.1	0	6354.45	6388.43	0.53
	UCS-4	1	8.3	813	0	142.1	0	5510.30	5304.37	3.88
	UCS-5	1	6.2	359	0	142.1	0	3186.18	3042.26	4.73
Ma et al. [19]	CESC-1	1	3	235	235	34	30	1694.59	1700.43	0.34
	CESC-2	1	2	235	235	34	30	2197.75	2167.51	1.40
Guo et al. [32]	S28-25a	1.98	2.6	235	0	34	25	944.62	953.79	0.96
	S28-50a	1.96	1.6	235	0	34	50	764.21	728.60	4.89
	S10-80a	1.51	2.6	235	0	34	0	1294.52	1224.33	5.50
	S20-50a	2.05	2.5	235	0	34	0	2506.65	2454.26	2.13
Yang et al. [9]	L-Ma-35-25	1.97	2.5	376.4	0	48.87	25	836.25	840.13	0.46
	L-Ma-35-50	1.92	2.6	376.4	0	48.87	50	638.81	639.54	0.11
	L-Ma-50-25	1.95	2.6	376.4	0	48.87	25	648.76	638.62	1.59
	L-Ma-50-50	1.95	2.6	376.4	0	48.87	50	529.15	538.74	1.78
Luo et al. [31]	UCFST-1	1	6.2	1153	0	146.3	14	3762	3810.36	1.26
	UCFST-2	1	6.2	1153	0	146.3	42	2501	2479.02	0.88
	UCFST-3	1	6.2	1153	0	146.3	84	1757	1694.94	3.39

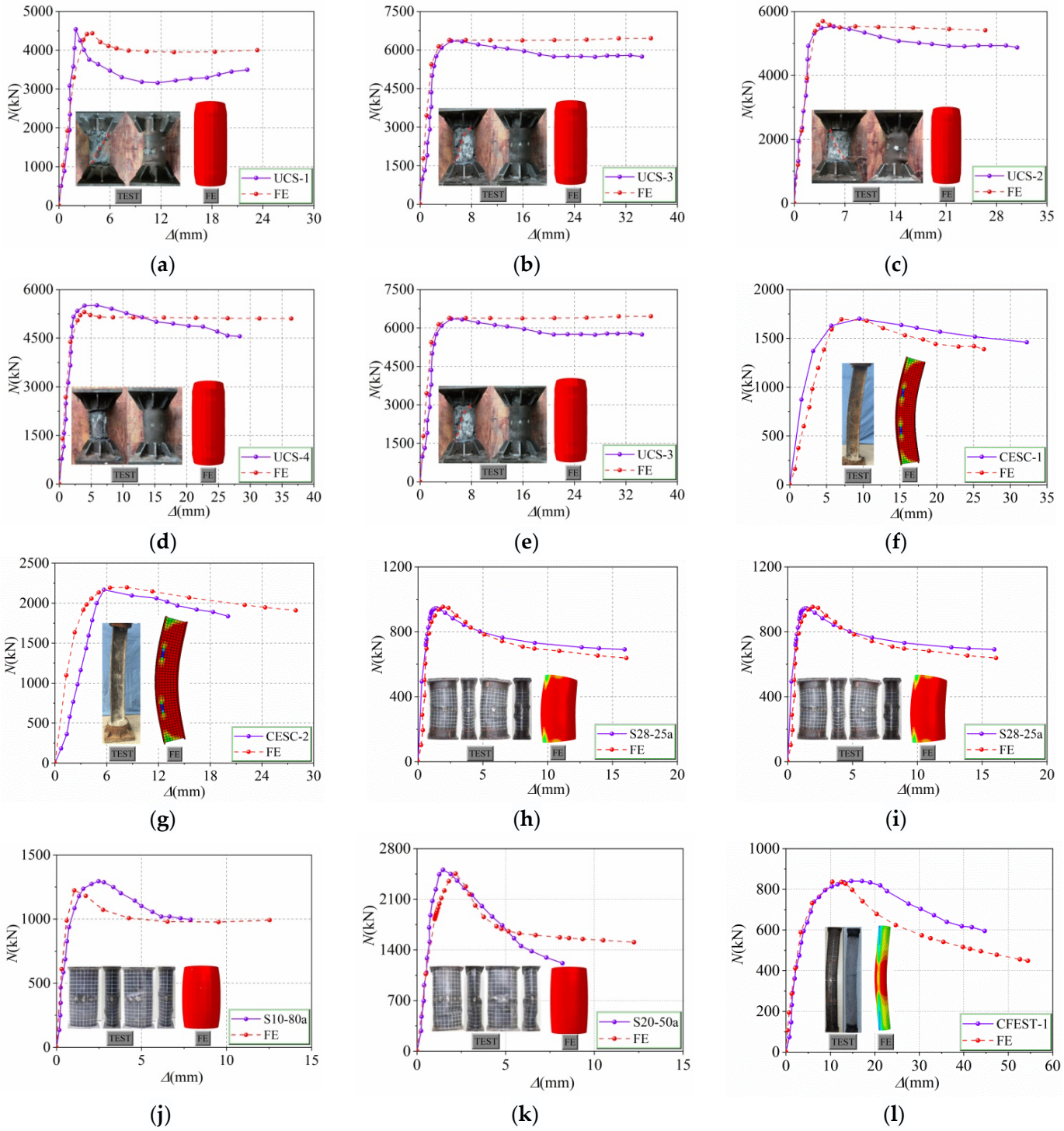

Figure 3. *Cont.*

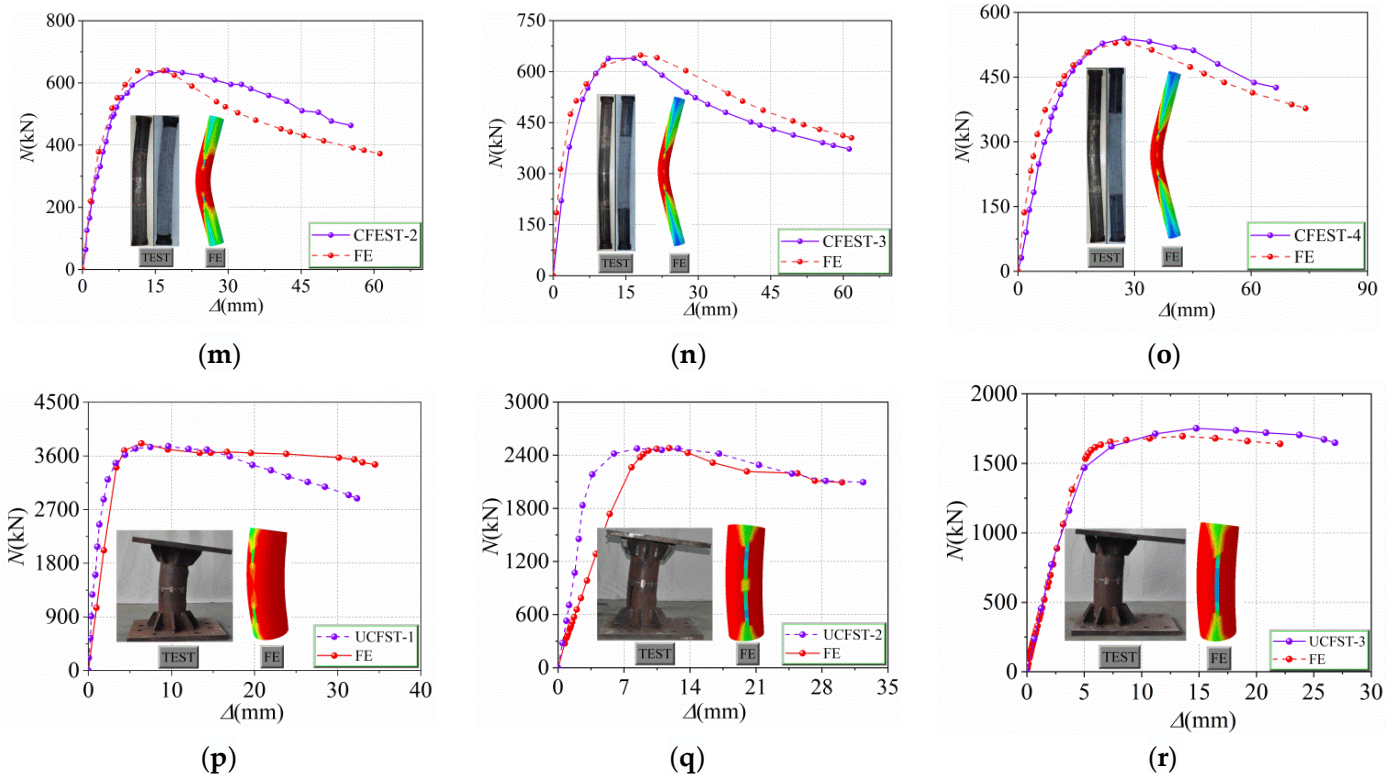

Figure 3. Comparisons for load–displacement curves between simulation and test results: (**a**) UCS-1; (**b**) UCS-2; (**c**) UCS-3; (**d**) UCS-4; (**e**) UCS-5; (**f**) CESC-1; (**g**) CESC-2; (**h**) S25-25 a; (**i**) S28-50 a; (**j**) S10-80 a; (**k**) S20-50 a; (**l**) L-Ma-35-25; (**m**) L-Ma-35-50; (**n**) L-Ma-50-25; (**o**) L-Ma-50-50; (**p**) UCFST-1; (**q**) UCFST-2; (**r**) UCFST-3.

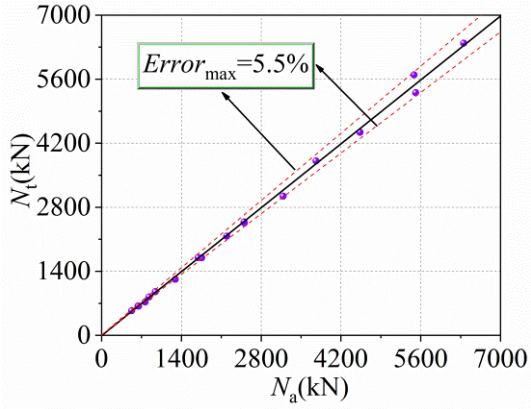

Figure 4. Compression between N_a and N_t for 18 test specimens.

5. Parameter Analysis

Figures 5–12 show the load–deflection curves of the 44 HUCFESTCs under eccentric loading. The main variable parameters are: (1) steel tube strength f_y (from 500 to 700 MPa); (2) thickness of the steel tube t (from 2 to 8 mm); (3) yield strength f_{y1} of the H-shape steel (from 500 to 700 MPa); (4) eccentricity e (from 30 to 70 mm); (5) cube compressive strength of the concrete f_{cu} (from 100 to 135 MPa); (6) slenderness ratio λ (from 2 to 3); (7) section area of the H-shape steel A_{HS} (from 680 to 1180 mm^2); (8) long–short axis ratio ψ (from 1 to 2).

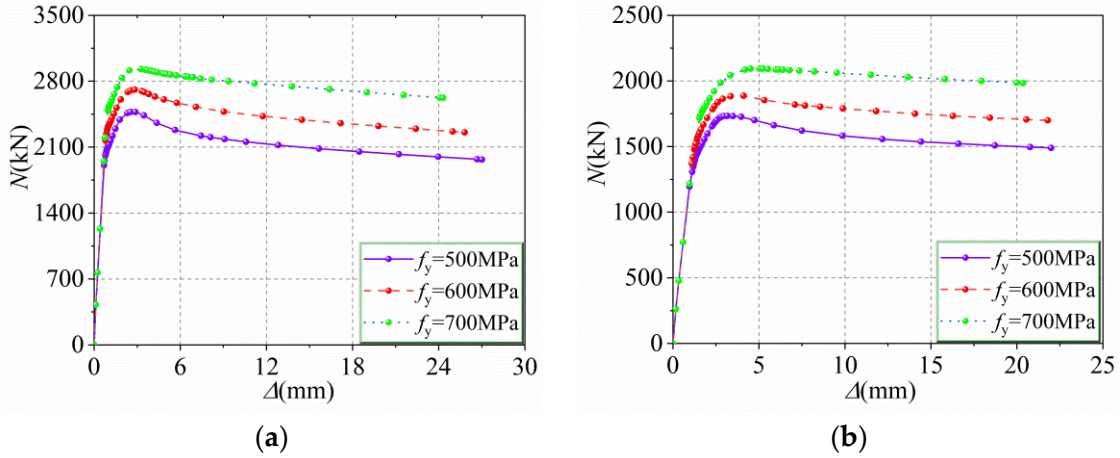

Figure 5. Curves of load–deflection for specimens with various f_y: (**a**) e = 20 mm; (**b**) e = 50 mm.

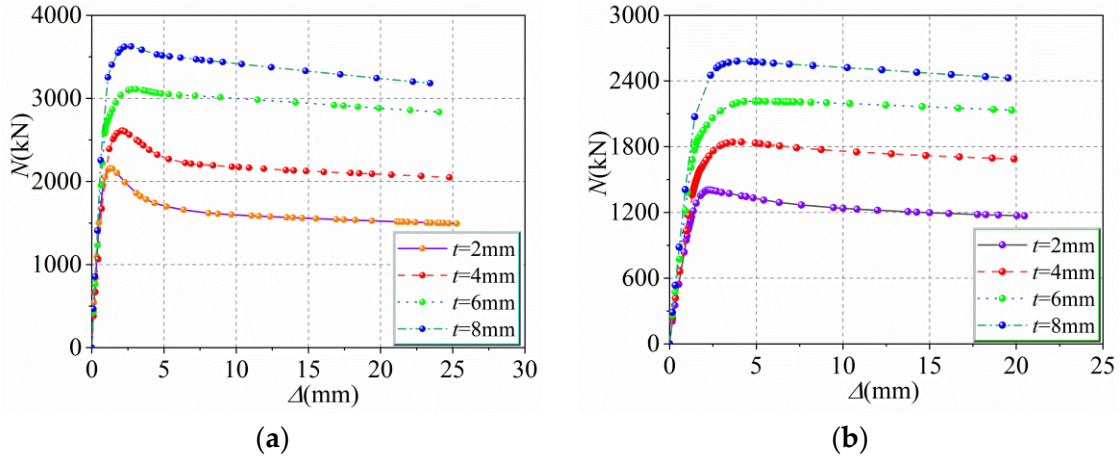

Figure 6. Curves of load–deflection for specimens with various t: (**a**) e = 20 mm; (**b**) e = 50 mm.

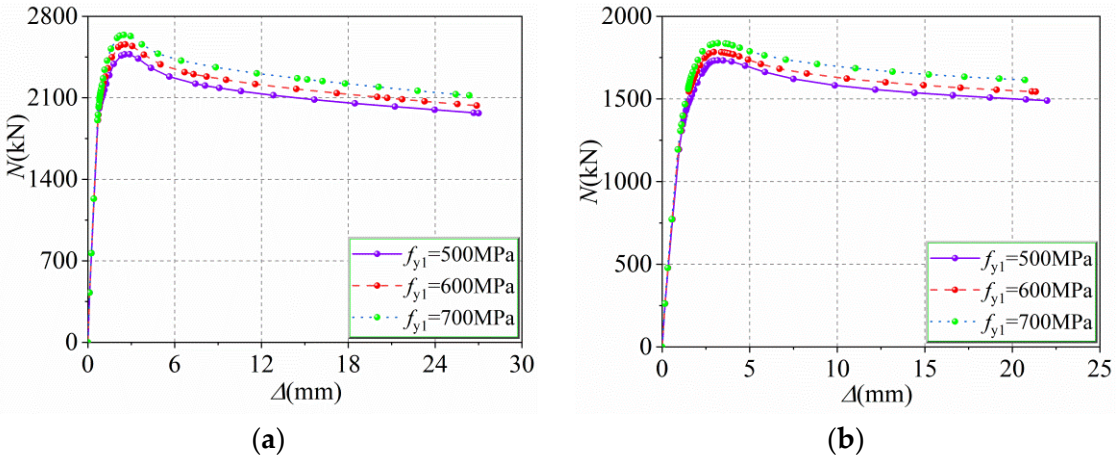

Figure 7. Curves of load–deflection for specimens with various f_{y1}: (**a**) e = 20 mm; (**b**) e = 50 mm.

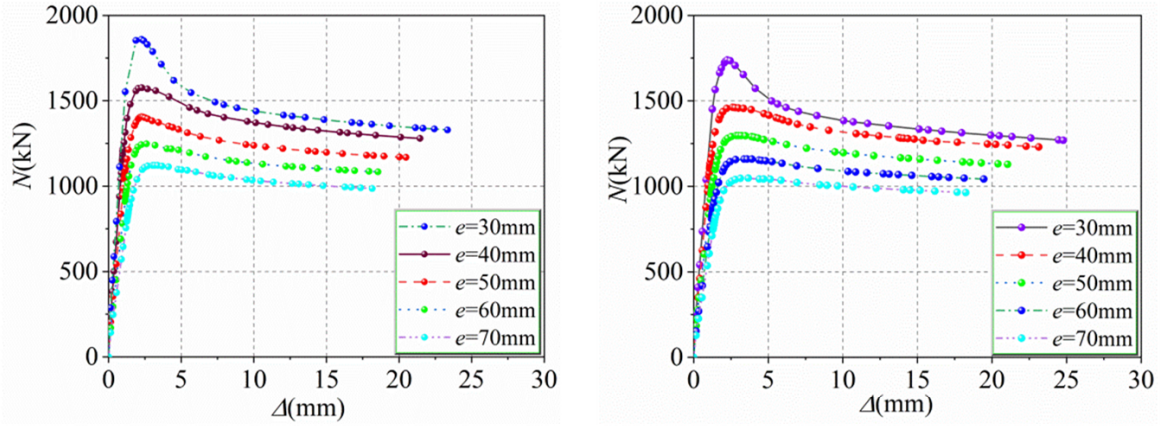

Figure 8. Curves of load–deflection for specimens with various e: (**a**) f_{cu} = 120 MPa; (**b**) f_{cu} = 100 MPa.

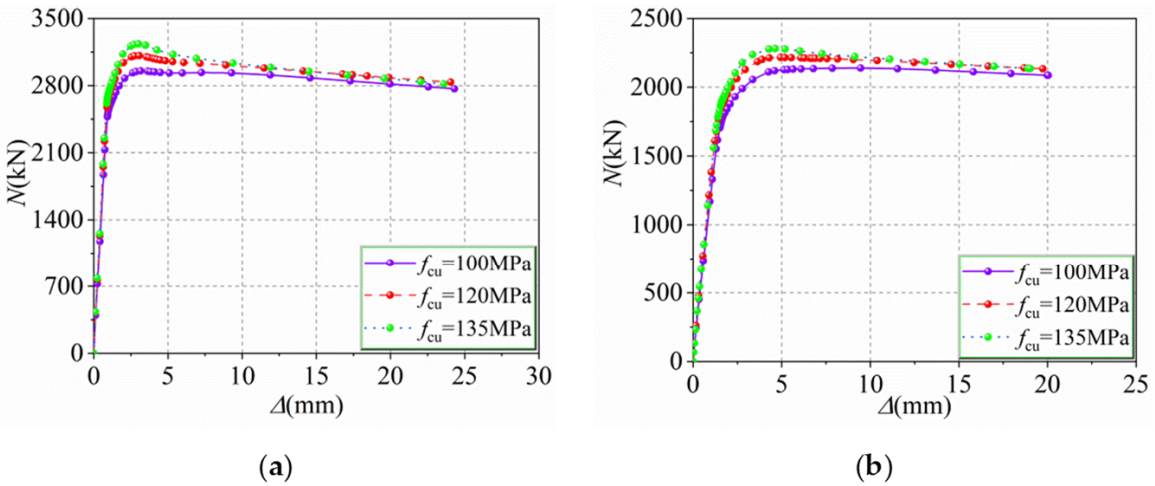

Figure 9. Curves of load–deflection for specimens with various f_{cu}: (**a**) e = 30 mm; (**b**) e = 50 mm.

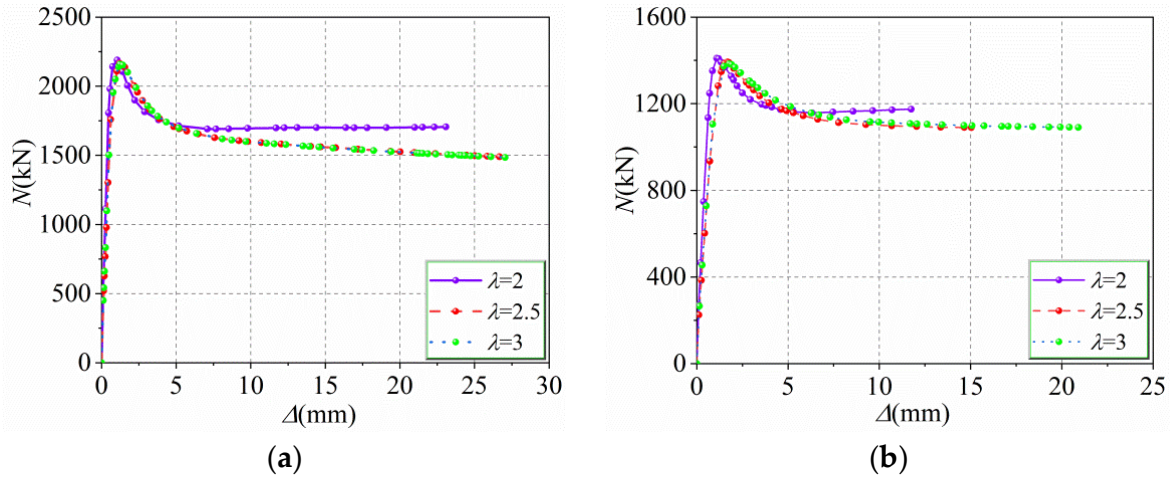

Figure 10. Curves of load–deflection for specimens with various λ: (**a**) e = 20 mm; (**b**) e = 50 mm.

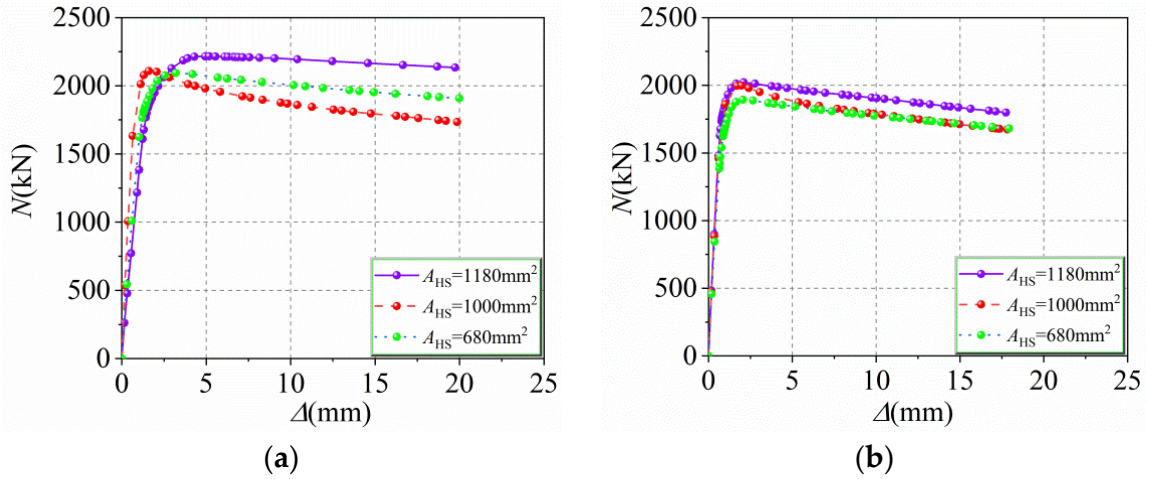

Figure 11. Curves of load–deflection for specimens with various A_{HS}: (**a**) e = 50 mm; (**b**) e = 60 mm.

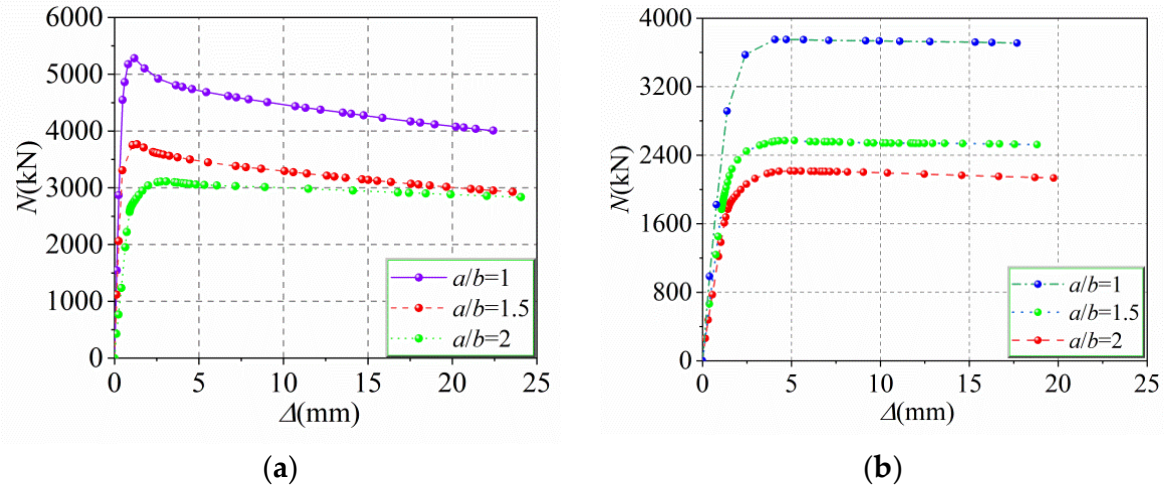

Figure 12. Curves of load–deflection for specimens with various ψ: (**a**) e = 20 mm; (**b**) e = 50 mm.

5.1. Steel Tube Yield Strength f_y (from 500 to 700 MPa)

As shown in Figure 5a, when f_y increases from 500 to 600 and 700 MPa, with an eccentricity of 20 mm, N_a of the HUCFESTCs increases from 2473.18 to 2700.65 and 2928.2 kN, respectively, increasing by 8.5% and 15.6%. In contrast, the middle cross-section deflection decreases from 21.98 to 21.79 mm and then to 20.36 mm, respectively, which correspond to decreases of 1.1%, 3.6%, and 7.4%. As seen in Figure 5b, when f_y increases from 500 to 600 and 700 MPa, with an eccentricity of 50 mm, N_a of the HUCFESTCs increases from 1733.04 to 1886.88, and 2093.60 kN, respectively, corresponding to increases of 8.2% and 17.3%. In contrast, the middle cross-section deflection decreases from 27.01 to 25.80 and 24.29 mm, respectively, which correspond to decreases of 4.5% and 10.1%. Figure 5 shows that with the increase in f_y, N_a of the HUCFESTCs increases, while the middle cross-section deflection decreases gradually, and the curves drop more slowly after peak load.

5.2. Thickness of Steel Tube t (from 2 mm to 8 mm)

As shown in Figure 6a, when t increases from 2 to 4, 6, and 8 mm, with an eccentricity of 20 mm, N_a of the HUCFESTCs improves from 2158.57 to 2611.29, 3111.3, and 3624.47 kN, respectively, which correspond to increases of 17.4%, 31.1%, and 41.5%. In contrast, the middle cross-section deflection decreases from 25.27 to 24.77, 24.05, and 23.43 mm, respectively, which correspond to decreases of 2%, 4.9%, and 7.3%. As seen in Figure 6b, when t increases from 2 to 4, 6, and 8 mm, with an eccentricity of 50 mm, N_a of the HUCFESTCs

improves from 1405.88 to 1843.24, 2215.83, and 2580.67 kN, respectively, which correspond to increases of 24.1%, 37.5%, and 46.7%. In contrast, the middle cross-section deflection decreases from 20.48 to 19.87, 19.38, and 19.15 mm, respectively, corresponding to decreases of 3%, 5.4%, and 6.5%. Figure 6 shows that with the increase in t, N_a of the HUCFESTCs increases, obviously, and the load-holding capacity increases progressively, while the middle cross-section deflection decreases gradually, and the curves drop more slowly after peak load, so the lateral stiffness of the specimens can be improved by increasing t.

5.3. Yield Strength f_{y1} of H-Shape Steel (from 500 to 700 MPa)

As shown in Figure 7a, when f_{y1} increases from 500 to 600 and 700 MPa, with an eccentricity of 20 mm, N_a of the HUCFESTCs improves from 2473.18 to 2558.62, 2639.91 kN, respectively, which correspond to increases of 3.4% and 6.3%. In contrast, the middle cross-section deflection decreases from 27.01 to 26.88, and 26.34 mm, respectively, which correspond to decreases of 3% and 5.8%. As seen in Figure 7b, when f_{y1} increases from 500 to 600 and 700 MPa, with an eccentricity of 50 mm, N_a of the HUCFESTCs improves from 1733.04 to 1783.10 and 1837.25 kN, respectively, which correspond to increases of 2.9% and 5.7%. In contrast, the middle cross-section deflection decreases from 21.98 to 21.34 and 20.07 mm, respectively, corresponding to decreases of 3% and 5.8%. Figure 7 shows that with the increase in f_{y1}, N_a of the HUCFESTCs increases, obviously, while the middle cross-section deflection decreases gradually, so the lateral stiffness of the specimens can be improved by increasing $f_{y1.}$

5.4. Eccentricity e (from 30 to 70 mm)

As shown in Figure 8a, when e increases from 30 to 40, 50, 60, and 70 mm, with an f_{cu} of 120 MPa, N_a of specimens decreases from 1859.27 to 1576.21, 1405.38, 1247.5, and 1121.61 kN, respectively, which correspond to decreases of 15.3%, 24.5%, 32.9%, and 39.7%. The middle cross-section deflection decreases from 23.33 to 21.44, 20.48, 18.55, and 18.15 mm, respectively, which correspond to decreases of 8.2%, 12.3%, 20.5%, and 22.3%. As seen in Figure 8b, when e increases from 30 to 40, 50, 60, and 70 mm, with a f_{cu} of 100 MPa, N_a of specimens decreases from 1738.27 to 1459.46, 1297.01, 1159.06, and 1047.21 kN, respectively, which correspond to decreases of 16.1%, 25.4%, 33.4%, and 39.8%. The middle cross-section deflection decreases from 23.33 to 21.44, 20.48, 18.55, and 18.15 mm, which correspond to decreases of 8.2% and 12.3%, 20.5%, and 22.3%, respectively. Figure 8 shows that with the increase in e, N_a of the HUCFESTCs decreases gradually, and the middle cross-section deflection decreases accordingly.

5.5. Cube Compressive Strength of Concrete f_{cu} (from 100 to 135 MPa)

As shown in Figure 9a, when f_{cu} increases from 100 to 120 and 135 MPa, with an eccentricity of 20 mm, N_a of the HUCFESTCs improves from 2951.78 kN to 3111.3 kN and 3233.74 kN, respectively, which correspond to increases of 5.2% and 8.8%. In contrast, the middle cross-section deflection decreases from 24.31 to 24.05 and 23.59 mm, respectively, which correspond to decreases of 1.1%, and 3.0%. As seen in Figure 9b, when f_{cu} increases from 100 to 120 and 135 MPa, with an eccentricity of 50 mm, N_a of specimens increases from 2138.67 to 2215.83, and 2280.12 kN, respectively, which correspond to increases of 3.5% and 6.3%. In contrast, the middle cross-section deflection decreases from 20.03 to 19.3 and 19.02 mm, respectively, corresponding to decreases of 3.7% and 5.1%. Figure 9 shows that with the increase in f_{cu}, N_a of the HUCFESTCs increases gradually, and the middle cross-section deflection decreases accordingly.

5.6. Slenderness Ratio λ (from 2 to 3)

Figure 10a shows that when λ increases from 2 to 2.5 and 3, with an eccentricity of 20 mm, N_a of specimens decreases from 2188.73 to 2166.54, and 2150.57 kN, respectively, which correspond to decreases of 1.2% and 1.8%. The middle cross-section deflection increases from 23.08 to 26.67, and 27.04 mm, which correspond to increases of 13.5% and

14.7%. As seen in Figure 10b, when λ increases from 2 to 2.5 and 3, with an eccentricity of 50 mm, N_a of specimens decreases from 1409.5 to 1392.31, and 1384.54 kN, respectively, which correspond to decreases of 1.3% and 1.8%. The middle cross-section deflection increases from 11.74 to 15.03 and 20.90 mm, which correspond to increases of 21.9% and 44.9%. Figure 10 shows that with the increase in λ, N_a of the HUCFESTCs gradually decreases. In contrast, obviously, the lateral deflection increases.

5.7. Section Area of H-Shape Steel A_{HS} (from 680 to 1180 mm^2)

It can be seen from Figure 11a that when A_{HS} decreases from 1180 to 1000, and 680 mm^2, with an eccentricity of 50 mm, N_a of specimens decreases from 2215.83 to 2108.51, 2093.82 kN, respectively, which correspond to decreases of 4.9% and 5.6%. In contrast, the middle cross-section deflection increased from 19.73 to 19.86 and 19.98 mm, respectively, corresponding to increases of 0.7% and 1.3%. As shown in Figure 11b, when A_{HS} decreases from 1180, 1000,' and 680 mm^2, with an eccentricity of 60 mm, N_a of specimens decreases from 2012.77 to 1988.22, and 1889.25 kN, respectively, which correspond to decreases of 1.3% and 1.8%. In contrast, the middle cross-section deflection increases from 17.74 to 17.84, and 17.92 mm, respectively, which correspond to increases of 0.6% and 1.1%. Figure 11 shows that with the decrease in A_{HS}, N_a of the HUCFESTCs decreases, obviously, while the middle cross-section deflection gradually increases.

5.8. Long–Short Axis Ratio ψ (from 1 to 2)

It can be seen from Figure 11a that when ψ increases from 1, 1.5, and 2, with an eccentricity of 20 mm, N_a of specimens decreases from 5281.76 to 3766.03, and 3111.30 kN, respectively, which correspond to decreases of 29.7% and 42.1%. In contrast, the middle cross-section deflection increases from 22.42 to 23.57, and 24.05 mm, respectively, which correspond to increases of 4.9% and 6.9%. As shown in Figure 12b, when ψ increases from 1, 1.5, and 2, respectively, with an eccentricity of 50 mm, N_a of the specimens decreases from 3749.93 to 2570.45, and 2215.83 kN, respectively, which correspond to decreases of 31.5% and 41%. In contrast, the middle cross-section deflection increases from 17.68 to 18.81 and 19.3 mm, respectively, which correspond to increases of 6.1% and 8.4%. Figure 12 shows that with the increase in ψ, N_a of the HUCFESTCs decreases, obviously, while the middle cross-section deflection increases gradually. When the section of the HUCFESTCs is close to the circular section, N_a of the HUCFESTCs is greatly affected by ψ. In contrast, the influence of ψ on the eccentric ultimate bearing capacity decreases gradually with the increase in ψ.

6. Deformation Capacity of HUCFESTCs

6.1. Lateral Deflection Curves of HUCFESTCs

For the three typical specimens, i.e., HUCFEST-18 (e = 40 mm), HUCFEST-19 (e = 50 mm), and HUCFEST-20 (e = 60 mm), the lateral deflection curves are displayed on Figure 13. As shown in Figure 13, when the load gradually rises from zero to 0.88 N_a, less variation in lateral deflection occurs along the height of the HUCFESTCs; nevertheless, when the force gradually rises from 0.88 N_a to peak load, the deflection increases dramatically. The deflection curves are virtually in the shape of a half-sine wave when HUCFESTCs are subjected to eccentrical compression force. The development law of the HUCFESTCs lateral deflection curves is similar to that for ordinary CFSTCs.

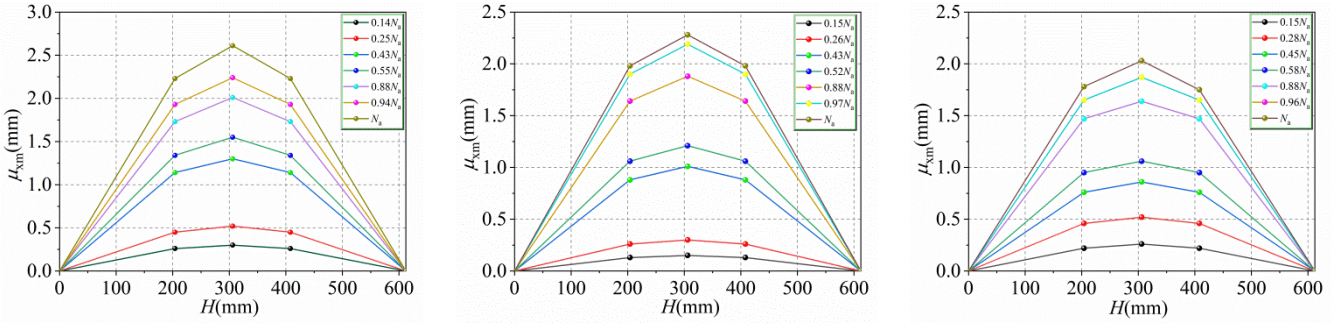

(**a**) (**b**) (**c**)

Figure 13. Lateral deflection curves for three typical specimens: (**a**) HUCFEST-18 (e = 40 mm); (**b**) HUCFEST-19 (e = 50 mm); (**c**) HUCFEST-20 (e = 60 mm).

6.2. Stiffness Degradation of Specimens

The stiffness of HUCFESTCs can be represented as:

$$EI = \frac{NeL^2}{\pi^2 \Delta} \tag{4}$$

where EI is the secant bending stiffness (kN·m^2), e is the eccentricity (mm), L is the overall height of the HUCFESTCs (mm), Δ is the middle cross-section deflection of the HUCFESTCs (mm), and N is the eccentric load (kN).

Figure 14 illustrates the stiffness degradation curves of specimens with various values as determined by Equation (4). EI in Figure 14 is secant stiffness and EI_0 is initial stiffness. During the initial loading stage, the specimens are in the elastic phase, and the stiffness is constant. The specimens enter the elastic–plastic stage as N increases, and the stiffness begins to decrease as the deflection increases. As shown in Figure 14a, with the yield strength increase, the steel tube's restraining effect on the concrete gradually increases, as do the ductility and stiffness of the specimens. It can be seen from Figure 14b that with the thickness of the steel tube, the restraining effect of the steel tube on the concrete is significantly enhanced, the ductility of the specimen is greatly improved, and the stiffness of the specimen is significantly increased. As seen in Figure 14c, with the increase in H-shape steel yield strength, the specimen ductility and stiffness increase gradually, and the magnitude of the increase is small. It can be seen from Figure 14d that with the increase in eccentricity, the ductility and stiffness of the specimens gradually increase. For HUCFESTCs, the influence of t and e on the bending stiffness is significant.

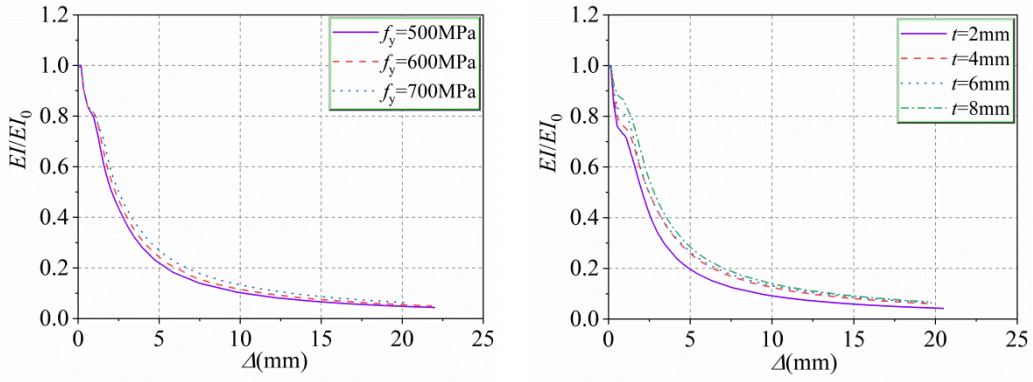

(**a**) (**b**)

Figure 14. *Cont.*

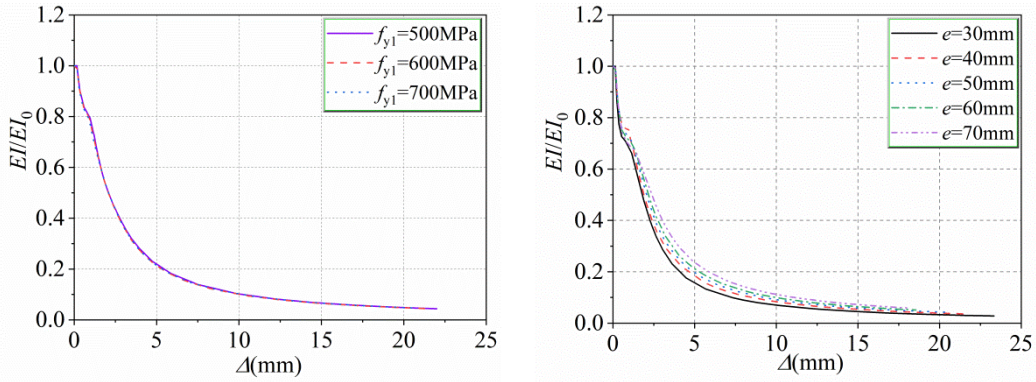

Figure 14. Stiffness degradation curves under different parameters: (**a**) f_y; (**b**) t; (**c**) f_{y1}; (**d**) e.

6.3. Load–Strain Curves of HUCFESTCs

For the three typical specimens, i.e., HUCFEST-18 (e = 40 mm), HUCFEST-19 (e = 50 mm), and HUCFEST-20 (e = 60 mm), the load–strain (N–ε) curves are displayed on Figure 15. Based on the assumption that tensile strain is positive and compressive strain is negative, at the initial loading stage, each component of the HUCFESTCs had a linear shift in strain, indicating that the HUCFESTCs were in the elastic phase. The specimen's longitudinal strain started to trend nonlinearly once it had achieved 95% of the peak load. The steel tube in all locations and the high-strength H-shape steel in the compression zone both attained yield strength when the specimen reached its maximum load. According to Figure 15, as specimens attain their maximum load, the eccentricity and drop rate of the load–strain curves steadily decrease as eccentricity increases. The HUCFESTCs features compression-controlled failure mode, high-strength steel tubes in all areas, and the compression zone of the H-shape steel can reach the yield strength.

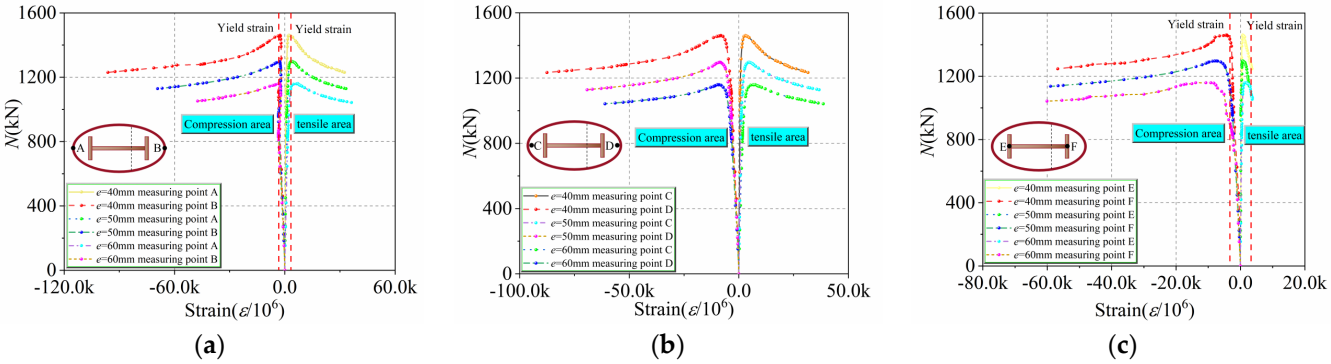

Figure 15. N–ε curves for various eccentricities: (**a**) steel tube; (**b**) concrete; (**c**) H-shape steel.

7. Verification of the Plane Section Assumption

Three representative specimens (HUCFEST-18 (e = 40 mm), HUCFEST-19 (e = 50 mm) and HUCFEST-20 (e = 60 mm)) were used to confirm the assumption of plane cross-section. The mid-span section's longitudinal strain distribution curves were created, as shown in Figure 16. At the initial loading stage, the section's longitudinal strain had no obvious difference under various loads. The strain changed linearly along with the section height, which indicates that the specimens met the plane section assumption. However, after the load reached 0.90 N_a, the longitudinal strain began to show a nonlinear relationship; this is because, with the gradual increase in the load, the steel tube in the mid-span section began to buckle locally. Thus, the coordination relationship between the steel tube and inner concrete was destroyed. It can be concluded that the section deformation did not follow the plane section assumption at the late loading stage.

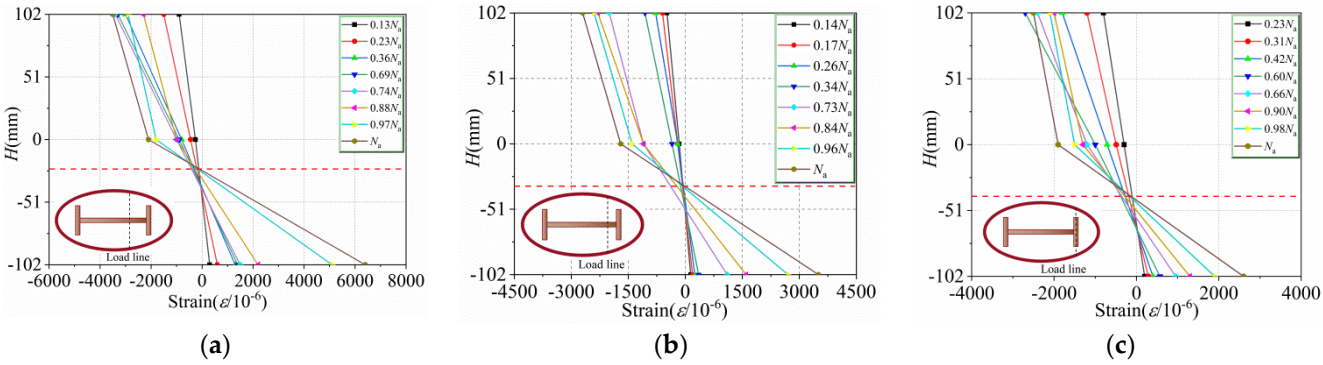

Figure 16. The mid-span section longitudinal strain distribution curves for three typical specimens: (**a**) HUCFEST-18; (**b**) HUCFEST-19; (**c**) HUCFEST-20.

8. Working Mechanism of HUCFESTCs

8.1. Contact Stress Analysis

Three typical specimens, i.e., HUCFEST-18 (e = 40 mm), HUCFEST-19 (e = 50 mm), and HUCFEST-20 (e = 60 mm) were selected from the 44 HUCFESTCs, and the contact stress between the steel tube and core concrete of the section for the specimens are presented in Figure 17. At the initial loading stage, the contact stress between the steel tube and concrete is 0 while the compression load increases. The contact stress grows progressively with increasing mid-span deflection. At the initial stage of the elastoplastic stage, after a faster growth, the contact stress tends to stabilize with a gradual increase in deflection. Figure 17a–c demonstrate interactions in the tension area of the compression area and between the concrete and steel tube of the medium section, and the interaction in the compression area is more significant. The binding force is predominantly focused near the end of the long axis of the elliptical section. Owing to the local bulging of the steel tube in the short-axis direction causes the contact stress at point C to be small. As shown in Figure 17d–f, there is inconsistent initial deformation between H-shape steel and concrete at the initial loading stage because of the different Poisson's ratio. With the gradual increase in load, the contact stress gradually increases. The contact stress of the H-shape steel in the compression area is always greater than in the tension area. In addition, the contact stress deflection curve of the H-shape steel in the compression area exhibits an obvious sudden drop because as the load increases, the H-shape steel reaches its yield strength, buckles inward, and temporarily disengages from the concrete in the compression area. After that, the concrete produces radial displacement, and the contact stress begins to increase gradually with the increase in deflection.

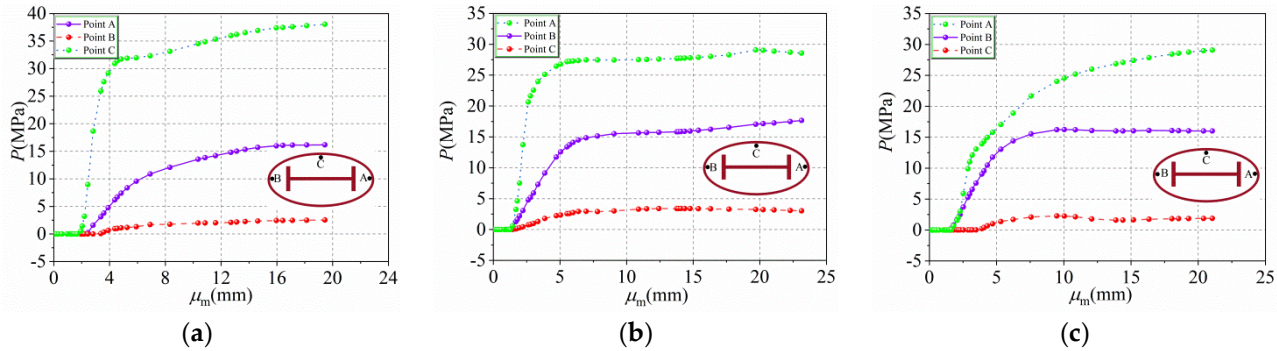

Figure 17. *Cont.*

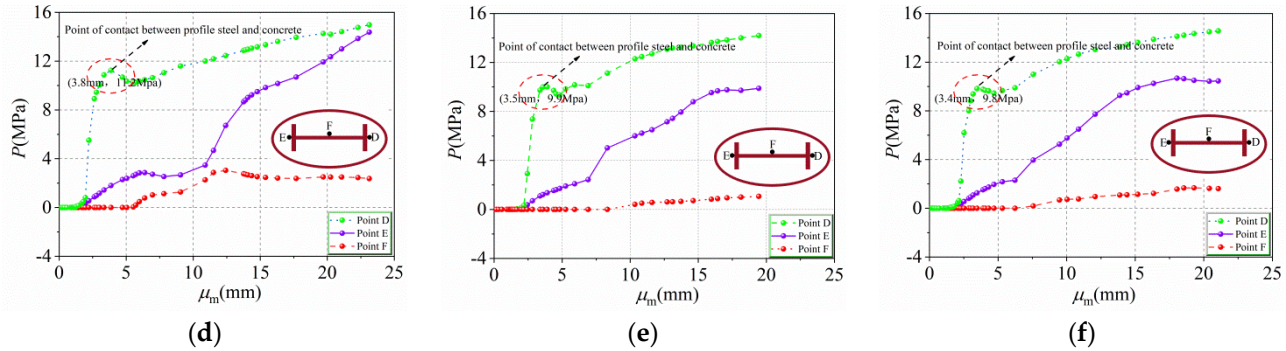

Figure 17. Contact stress curve of three typical specimens: (**a**) HUCFEST-18 contact stress curve between steel tube and concrete; (**b**) HUCFEST-19 contact stress curve between steel tube and concrete; (**c**) HUCFEST-20 contact stress curve between steel tube and concrete; (**d**) HUCFEST-18 contact stress curve between H-shape steel and concrete; (**e**) HUCFEST-19 contact stress curve between H-shape steel and concrete; (**f**) HUCFEST-20 contact stress curve between H-shape steel and concrete.

8.2. Failure Mechanism Analysis of HUCFESTCs

The components of the HUCFESTCs produce longitudinal strain (ε_1) as the eccentric load gradually increases. Moreover, with the generation of longitudinal strain, the components expand in the circumferential direction to produce radial strain (ε_s). The relationship expression between ε_1 and ε_s is given in Equation (5) [30]:

$$\begin{cases} \varepsilon_s = \mu_s \varepsilon_1 \\ \varepsilon_c = \mu_c \varepsilon_1 \end{cases} \tag{5}$$

where ε_s is the radial strain of the steel, ε_c is the radial strain of the concrete, μ_s is Poisson's ratio of the steel, and μ_c is Poisson's ratio of the concrete.

At the initial loading stage, steel tube, H-shape steel, and concrete have little contact and operate independently. During this stage, the longitudinal stress of steel tubes, H-shape steel, and concrete is distributed in strips. The steel tube and H-shape steel are in a compression condition because the stress on the compression side is greater than that on the tension side. At this stage, neither the steel tube nor the H-shape steel exerts any constraint on the concrete. With the increase in load, the steel tube and H-shape steel in the compression area reach the proportional limit, and Poisson's ratio of the steel and the concrete is roughly equivalent to the radial strain. Afterward, the specimen enters the elastoplastic phase. As the load increases gradually, the Poisson's ratio of the concrete is greater than that of the steel tube, and the radial strain of the concrete is greater than that of the steel tube and the H-shape steel in the compression zone. At this time, the steel tube and the H-shape steel begin to constrain the core concrete. The stress distribution of the three microelements is shown in Figure 18, and the steel tube is subjected to radial compression and circumferential tension, while both the H-shape steel and the concrete are under radial and circumferential compression. With the increase in load, the bearing capacity of the composite column reaches the extreme limit, and the plastic strain in the compression area of the steel tube and concrete begins to concentrate on the mid-span section and its two sides. In the compression zone of the H-shape steel, the plastic strain is concentrated at the mid-span flange.

As deflection gradually increases, the specimens enter the plastic stage. At this stage, the specimens' bearing capacity declines steadily as deflection increases. During the later loading stage, the steel tubes reach their yield strength, while the H-shape steel in the compression area also reaches its yield strength. Figure 19 depicts the longitudinal stress distributions of the H-shaped steel at various stages for the typical specimen HUCFEST-18 (f_y = 700 MPa, t = 2 mm, f_{y1} = 700 MPa, A_{HS} = 1180 mm^2, ψ = 2, f_{cu} = 100 MPa, λ = 3, and e = 50 mm).

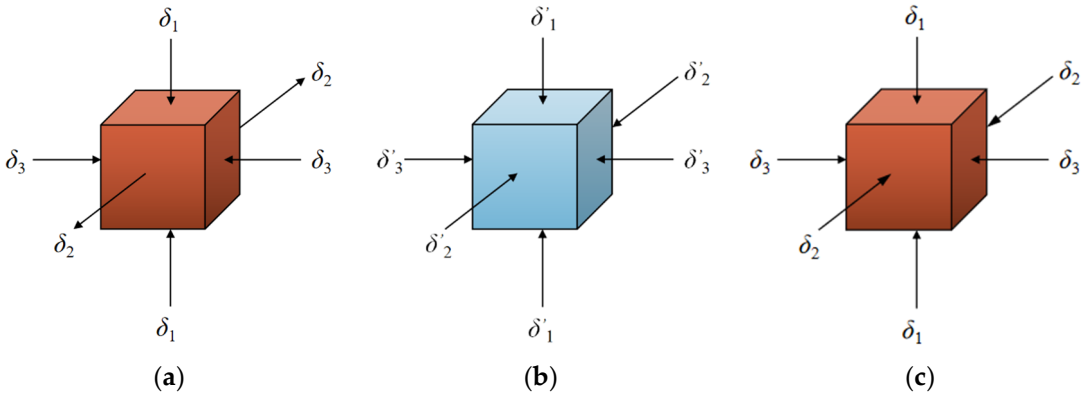

Figure 18. Schematic diagram of element microstress: (**a**) steel tube; (**b**) concrete; (**c**) H-shape steel.

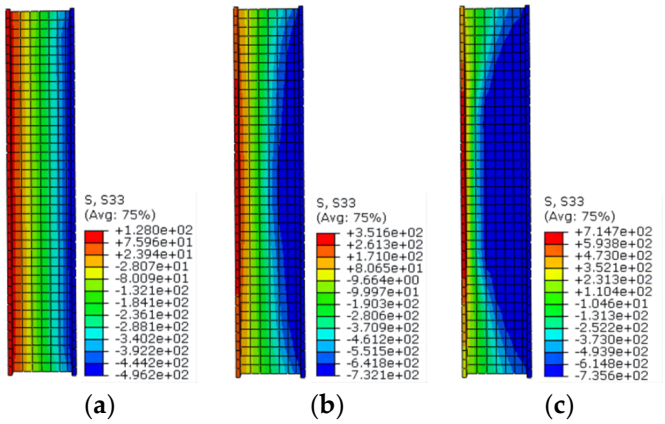

Figure 19. Longitudinal stress distribution of the H−shape steel at each stage for typical specimen HUCFEST-18: (**a**) elastic stage; (**b**) elastic-plastic stage; (**c**) plastic stage.

At this stage, the lateral expansion of the concrete has developed significantly; the contact stress between steel and concrete is gradually increasing, and the influence of the steel tube and section steel on the concrete is gradually increasing. At the later loading stage, the steel tube begins to bulge locally and part of the concrete in the compression area is crushed. The concrete damage pattern of typical specimen HUCFEST-18 is shown in Figure 20. It can be seen from Figure 20 that the contact part between the inner side of the mid-span steel section and the concrete and the end point of the long axis of the concrete compression area is the most visible. Figure 21a,b depict the final failure mode of typical specimen HUCFEST-18. As shown in Figure 21, the main failure mode of the steel tube is local bulging, and part of the concrete is crushed. The failure modes of the steel tube and concrete in the HUCFESTCs resemble those of the CFESTCs [9].

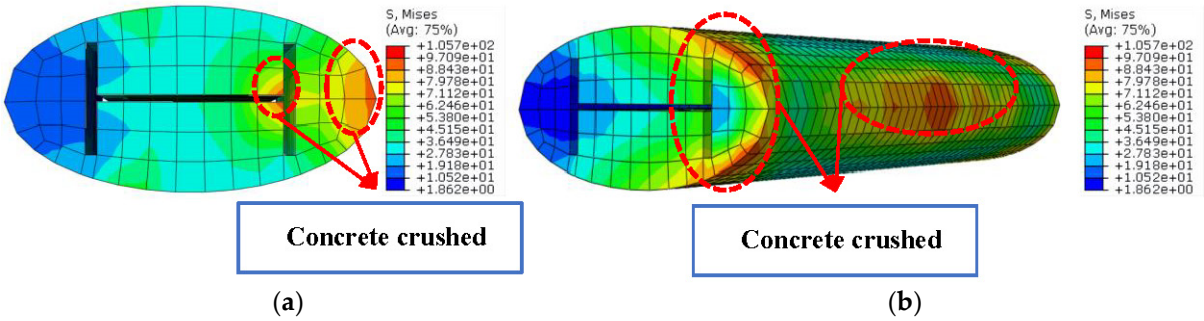

Figure 20. Concrete failure diagram for the finite element simulation of typical specimen HUCFEST-18: (**a**) crushed concrete on the inner side of the H-shape steel in the span section; (**b**) concrete of the compression area was crushed.

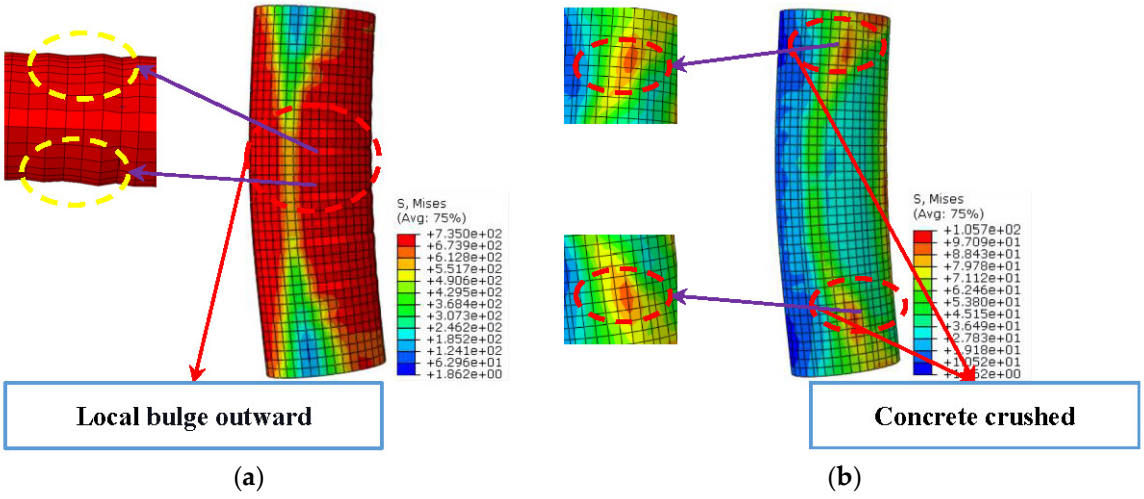

Figure 21. The final failure mode of typical specimen HUCFEST-18: (**a**) steel tubes; (**b**) concrete.

9. Bearing Capacity of HUCFESTCs Subjected to Eccentric Load

At present, the European Code EC4 [33] gives the ultimate bearing capacity formula of concrete-filled steel tube under axial compression using the simple superposition principle, as shown in Equation (6):

$$N_{EC4} = A_S f_y + A_c f_c \quad (6)$$

where A_S is the cross-sectional area of the steel tube, f_y is the yield strength of the steel tube, A_c is the cross-sectional area of the concrete, and f_c is the compressive strength of the concrete cylinder.

Guo [32] put forward the axial compression bearing capacity formula for CFEST composite columns, as shown in Equation (7), based on EC4, after carrying out an axial compression test of 24 CFEST composite columns:

$$N_{EC4\,S} = \left[1 + 4.9 + \left(\frac{t}{2a}\right) \times \left(\frac{b}{a}\right) \times \left(\frac{f_y}{f_{ck}}\right)\right] \times A_c \times f_c + 0.75\, A_S f_y \quad (7)$$

For the concrete-filled steel tube composite columns with H-shaped steel, the European Code EC4 uses the simple superposition principle to give the formula for the ultimate bearing capacity of the concrete-filled steel tube composite columns with H-shaped steel under axial load, as shown in Equation (8):

$$N_{EC4,HCFST} = A_S f_y + A_c f_c + A_{HS} f_{HS} \quad (8)$$

This paper combines the axial load ultimate bearing capacity of CFSTCs with section steel in EC4 and the axial load ultimate bearing capacity of the CFESTCs proposed by Guo [32]. By introducing the eccentric reduction coefficient φ, the eccentric bearing capacity of HUCFESTCs can be calculated by using Equations (9)–(11):

$$N_{\mathrm{u}} = \varphi \times \left\{ \left[1 + 4.9 \times \left(\frac{\mathrm{t}}{2\,a} \right) \times \left(\frac{b}{a} \right) \times \left(\frac{f_{\mathrm{y}}}{f_{\mathrm{ck}}} \right) \right] \times A_{\mathrm{c}} \times f_{\mathrm{c}} + 0.75 A_{\mathrm{S}} f_{\mathrm{y}} + A_{\mathrm{HS}} f_{\mathrm{y1}} \right\} \quad (9)$$

$$\varphi = -0.78\alpha^4 - 0.36\alpha^3 + 1.72\alpha^2 - 1.6\alpha + 0.89 \quad (10)$$

$$\alpha = e/a \quad (11)$$

where A_{S} is the cross-sectional area of the steel tube, f_{y} is the yield strength of the steel tube, A_{c} is the cross-sectional area of the concrete, f_{c} is the compressive strength of the concrete cylinder, A_{HS} is the sectional area of the H-shape steel, f_{y1} is the yield strength of the H-shape steel, φ is the eccentricity reduction coefficient, t is the thickness of the steel tube wall, a is the long axis radius, b is the short axis radius, and e is the eccentricity.

The bearing capacity to eccentric compression of the 44 HUCFESTCs, calculated according to Equation (9), is shown in Table 2, and the sum dispersion degree of the 44 HUCFESTCs is shown in Figure 22. It can be seen that the maximum error between N_{a} and N_{u} is 8.36%, which meets the engineering accuracy requirement. This formula is suitable for HUCFESTCs with an aspect ratio of 1–2 and a concrete strength of less than 135 MPa.

Table 2. Comparison between N_{a} and N_{u} for the 44 HUCFESTCs.

Specimen	$2a \times 2b$/mm	A_{HS}/mm^2	t/mm	α	φ	N_{a}/kN	N_{u}/kN	$\left\lvert \frac{N_{\mathrm{u}} - N_{\mathrm{a}}}{N_{\mathrm{u}}} \right\rvert \times 100\%$
HUCFEST-1	204 × 102	1180	6	0.5	0.47	1733.04	1658.32	4.50
HUCFEST-2	204 × 102	1180	6	0.5	0.47	1886.88	1796.13	5.00
HUCFEST-3	204 × 102	1180	6	0.5	0.47	2093.60	2033.94	2.87
HUCFEST-4	204 × 102	1180	6	0.2	0.70	2473.18	2487.48	0.58
HUCFEST-5	204 × 102	1180	6	0.2	0.70	2700.65	2694.19	0.22
HUCFEST-6	204 × 102	1180	6	0.2	0.70	2928.20	2900.91	0.93
HUCFEST-7	204 × 102	1180	6	0.5	0.47	1783.10	1713.38	0.47
HUCFEST-8	204 × 102	1180	6	0.5	0.47	1837.25	1768.45	0.52
HUCFEST-9	204 × 102	1180	6	0.2	0.70	2558.62	2570.08	4.06
HUCFEST-10	204 × 102	1180	6	0.2	0.70	2639.90	2652.68	3.88
HUCFEST-11	204 × 102	1180	2	0.3	0.6	1859.27	1958.35	5.07
HUCFEST-12	204 × 102	1180	2	0.4	0.53	1576.21	1540.75	2.28
HUCFEST-13	204 × 102	1180	2	0.5	0.47	1405.38	1503.16	6.53
HUCFEST-14	204 × 102	1180	2	0.6	0.41	1247.50	1241.83	0.49
HUCFEST-15	204 × 102	1180	2	0.7	0.33	1121.61	1087.97	3.04
HUCFEST-16	204 × 102	1180	2	0.3	0.6	1738.27	1787.78	2.78
HUCFEST-17	204 × 102	1180	2	0.4	0.53	1459.46	1489.14	2.02
HUCFEST-18	204 × 102	1180	2	0.5	0.47	1297.01	1390.49	6.72
HUCFEST-19	204 × 102	1180	2	0.6	0.41	1159.06	1224.96	5.38
HUCFEST-20	204 × 102	1180	2	0.7	0.33	1047.21	993.21	5.42
HUCFEST-21	204 × 102	1180	4	0.5	0.47	1843.24	1792.80	2.80
HUCFEST-22	204 × 102	1180	8	0.5	0.47	2580.67	2477.55	4.00
HUCFEST-23	204 × 102	1180	2	0.2	0.70	2158.57	2284.74	5.55
HUCFEST-24	204 × 102	1180	4	0.2	0.70	2611.29	2689.20	2.91
HUCFEST-25	204 × 102	1180	6	0.2	0.70	3111.30	3066.11	1.46
HUCFEST-26	204 × 102	1180	8	0.2	0.70	3624.47	3416.33	6.08
HUCFEST-27	204 × 102	1180	6	0.5	0.47	2138.67	2128.42	5.25
HUCFEST-28	204 × 102	1180	6	0.5	0.47	2215.83	2044.07	8.36

Table 2. *Cont.*

Specimen	2a × 2b/mm	A_{HS}/mm^2	*t*/mm	α	φ	N_a/kN	N_u/kN	$\left\|\frac{N_u-N_a}{N_u}\right\|\times 100\%$
HUCFEST-29	204 × 102	1180	6	0.5	0.47	2280.12	2330.81	2.15
HUCFEST-30	204 × 102	1180	6	0.2	0.70	2951.78	2892.63	2.02
HUCFEST-31	204 × 102	1180	6	0.2	0.70	3233.47	3196.22	1.15
HUCFEST-32	204 × 102	1180	2	0.5	0.47	1392.31	1423.16	2.20
HUCFEST-33	204 × 102	1180	2	0.5	0.47	1384.54	1423.16	1.80
HUCFEST-34	204 × 102	1180	2	0.2	0.70	2188.73	2284.74	4.23
HUCFEST-35	204 × 102	1180	2	0.2	0.70	2166.45	2284.74	5.20
HUCFEST-36	204 × 204	1180	2	0.5	0.47	3749.93	3933.10	4.68
HUCFEST-37	204 × 136	1180	2	0.5	0.47	2570.45	2734.19	6.12
HUCFEST-38	204 × 204	1180	2	0.5	0.47	5281.76	5073.21	3.95
HUCFEST-39	204 × 136	1180	2	0.2	0.70	3766.03	3689.50	2.04
HUCFEST-40	204 × 102	1000	6	0.5	0.47	2108.15	2215.45	5.09
HUCFEST-41	204 × 102	680	6	0.5	0.47	2093.82	2100.72	0.33
HUCFEST-42	204 × 102	1180	6	0.6	0.41	2012.77	1989.33	1.16
HUCFEST-43	204 × 102	1000	6	0.6	0.41	1988.22	1955.60	1.64
HUCFEST-44	204 × 102	680	6	0.6	0.41	1899.25	1854.26	2.37

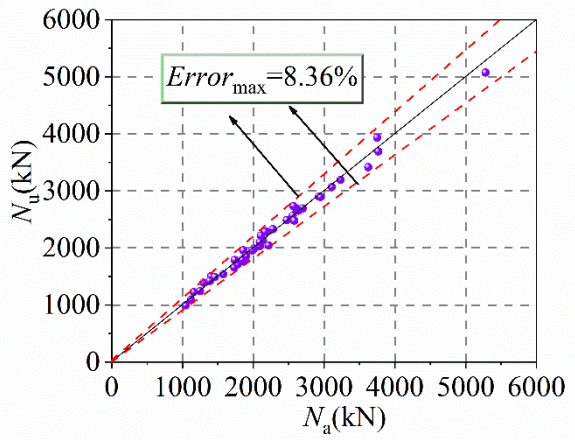

Figure 22. Comparison between N_a and N_t for the 44 HUCFESTCs.

10. Conclusions

ABAQUS software establishes the FE models of 44 HUCFESTCs under eccentrical compression loading. The load–deflection curves of the HUCFESTCs are recorded and the impact of different parameters on the ultimate eccentric load bearing capacity of HUCFESTCs is explored. The following precise conclusions can be drawn:

1. With the increase in f_y, t, f_{y1}, A_{HS}, and f_{cu}, the bearing capacity to eccentric load of the HUCFESTCs gradually increases, and the middle cross-section deflection of the specimens decreases progressively, among which f_y and t have the most significant effect. With increasing e, λ, and ψ, the bearing capacity to eccentric load of the HUCFESTCs gradually decreases. The change law of ultimate bearing capacity of the HUCFESTCs under eccentric load is similar to that of CFESTCs. At the same time, owing to the high strength of section steel and steel tube, the HUCFESTCs not only have high bearing capacity, but also have no lower ductility than the CFESTCs.
2. The deformation trend of the HUCFESTCs subjected to eccentric load is similar to that of ordinary CFESTCs, and their stiffness increases gradually with the increase in f_y, f_{y1}, t, and e, among which the eccentric distance and wall thickness have more influence on the stiffness of the HUCFESTCs. At the beginning of loading, the

HUCFESTCs conform to the assumption of a flat section, and with the increase in load, the deformation of the mid-span section is larger; HUCFESTCs do not conform to the assumption of a flat section.

3. The main failure mode of the HUCFESTCs subjected to eccentric load is a local buckling of the steel tube; the concrete in the compression zone and the inner side of the H-shape steel is crushed and the H-shape steel buckled.
4. An eccentricity discount factor is presented based on the formula for the ultimate bearing capacity of CFESTCs under axial compression stress, and statistical regression is then used to propose the formula for HUCFESTCs under eccentrical load. The maximum error is 8.36%, which can meet the demand for engineering accuracy.

Author Contributions: Conceptualization, J.J.; software, W.W.; validation, H.R. and Q.W.; writing—original draft, J.J., W.W. and L.J.; writing—review and editing, W.X. and Y.L. All authors have read and agreed to the published version of the manuscript.

Funding: This work is supported by China–Pakistan Belt and Road Joint Laboratory on Smart Disaster Prevention of Major Infrastructures, grant number 2022 CPBRJL-05; The Natural Science Foundation of Heilongjiang Province, grant number LH2020 E018; 2021 Social Science Development Research Project of Hebei Province, grant number 20210301135; Humanities and Social Science Research Project of Higher Education Institutions of Hebei Province, grant number SQ2021115; The Northeast Petroleum University Guided Innovation Fund, grant number 2020 YDL-02; and Guiding Science and Technology Project of Daqing City, grant number zd-2021-40.

Institutional Review Board Statement: Not applicable.

Informed Consent Statement: Not applicable.

Data Availability Statement: The raw data supporting the conclusion of this article will be made available by the authors, without undue reservation.

Conflicts of Interest: The authors declare no conflict of interest. The funders had no role in the design of the study; in the collection, analyses, or interpretation of data; in the writing of the manuscript, or in the publish the results.

References

1. Zhao, X.; Packer, J. Tests and design of concrete-filled elliptical hollow section stub columns. *Thin-Walled Struct.* **2009**, *47*, 617–628. [CrossRef]
2. Zhang, T.; Gong, Y.-Z.; Ding, F.-X.; Liu, X.-M.; Yu, Z.-W. Experimental and numerical investigation on the flexural behavior of concrete-filled elliptical steel tube (CFET). *J. Build. Eng.* **2021**, *41*, 102412. [CrossRef]
3. Pourbaba, M.; Joghataie, A.; Mirmiran, A. Shear behavior of ultra-high performance concrete. *Constr. Build. Mater.* **2018**, *183*, 554–564. [CrossRef]
4. Sohail, M.G.; Kahraman, R.; Al Nuaimi, N.; Gencturk, B.; Alnahhal, W. Durability characteristics of high and ultra-high performance concretes. *J. Build. Eng.* **2020**, *33*, 101669. [CrossRef]
5. Alsalman, A.; Dang, C.; Prinz, G.S.; Hale, W.M. Evaluation of modulus of elasticity of ultra-high performance concrete. *Constr. Build. Mater.* **2017**, *153*, 918–928. [CrossRef]
6. Jiang, L.Q.; Song, H.Y.; Ji, J. Axial compression behavior of GFRP tube reactive powder concrete composite columns with encased steel. *J. Northeast. Pet. Univ.* **2021**, *45*, 3.
7. Ji, J.; He, L.; Jiang, L.; Ren, H.; Ni, S.; Wang, Z.; Li, Y.; Yu, C.; Lin, Y. Seismic Behavior of GFRP Tube Reactive Powder Concrete Composite Columns With Encased Steel. *Front. Mater.* **2021**, *8*, 516. [CrossRef]
8. Sheehan, T.; Dai, X.; Chan, T.; Lam, D. Structural response of concrete-filled elliptical steel hollow sections under eccentric compression. *Eng. Struct.* **2012**, *45*, 314–323. [CrossRef]
9. Yang, H.; Liu, F.; Chan, T.-M.; Wang, W. Behaviours of concrete-filled cold-formed elliptical hollow section beam-columns with varying aspect ratios. *Thin-Walled Struct.* **2017**, *120*, 9–28. [CrossRef]
10. Hassanein, M.; Patel, V.; El Hadidy, A.; Al Abadi, H.; Elchalakani, M. Structural behaviour and design of elliptical high-strength concrete-filled steel tubular short compression members. *Eng. Struct.* **2018**, *173*, 495–511. [CrossRef]
11. Ipek, S.; Erdoğan, A.; Güneyisi, E.M. Compressive behavior of concrete-filled double skin steel tubular short columns with the elliptical hollow section. *J. Build. Eng.* **2021**, *38*, 102200. [CrossRef]
12. Guler, S.; Çopur, A.; Aydogan, M. Axial capacity and ductility of circular UHPC-filled steel tube columns. *Mag. Concr. Res.* **2013**, *65*, 898–905. [CrossRef]

13. Wei, J.G.; Luo, X.; Ou, Z.J.; Chen, B.C. Experiment Study on Axial Compressive Behavior of Circular UHPC Filled high-strength Tube Stub Columns. *J. Build. Strustures* **2020**, *11*, 41. [CrossRef]
14. Wei, J.G.; Xie, Z.T.; Luo, X.; Yang, Y.; Wu, Q.X.; Chen, B.C.; Yuan, Y. Behavior of circular steel tube confined ultra high performance concrete stub columns under axial compressive loading. *J. Build. Strustures* **2021**, *43*, 34. [CrossRef]
15. Ji, J.; Zeng, W.; Wang, R.; Ren, H.; Zhang, L.; Liu, Y.; Jiang, L.; He, L.; Lin, Y.; Yu, C. Bearing Capacity of Hollow GFRP Pipe-Concrete-High Strength Steel Tube Composite Long Columns Under Eccentrical Compression Load. *Front. Mater.* **2021**, *8*, 402. [CrossRef]
16. Ji, J.; Yu, C.; Jiang, L.; Zhan, J.; Ren, H.; Hao, S.; Fan, S.; Jiang, L.; Lin, Y.; He, L. Bearing Behavior of H-Shaped Honeycombed Steel Web Composite Columns with Rectangular Concrete-Filled Steel Tube Flanges under Eccentrical Compression Load. *Adv. Civ. Eng.* **2022**, *2022*, 2965131. [CrossRef]
17. Ma, H.; Chen, Y.; Bai, H.; Zhao, Y. Eccentric compression performance of composite columns composed of RAC-filled circular steel tube and profile steel. *Eng. Struct.* **2019**, *201*, 109778. [CrossRef]
18. Liao, J.; Li, Y.-L.; Ouyang, Y.; Zeng, J.-J. Axial compression tests on elliptical high strength steel tubes filled with self-compacting concrete of different mix proportions. *J. Build. Eng.* **2021**, *40*, 102678. [CrossRef]
19. Uenaka, K. Experimental study on concrete-filled elliptical/oval steel tubular stub columns under compression. *Thin-Walled Struct.* **2014**, *78*, 131–137. [CrossRef]
20. Dai, X.; Lam, D. Numerical modelling of the axial compressive behaviour of short concrete-filled elliptical steel columns. *J. Constr. Steel Res.* **2010**, *66*, 931–942. [CrossRef]
21. Ren, Q.-X.; Han, L.-H.; Lam, D.; Li, W. Tests on elliptical concrete filled steel tubular (CFST) beams and columns. *J. Constr. Steel Res.* **2014**, *99*, 149–160. [CrossRef]
22. Du, J.; Meng, W.; Khayat, K.H.; Bao, Y.; Guo, P.; Lyu, Z.; Abu-Obeidah, A.; Nassif, H.; Wang, H. New development of ultra-high-performance concrete (UHPC). *Compos. Part B Eng.* **2021**, *224*, 109220. [CrossRef]
23. Ullah, R.; Qiang, Y.; Ahmad, J.; Vatin, N.I.; El-Shorbagy, M.A. Ultra-High-Performance Concrete (UHPC): A State-of-the-Art Review. *Materials* **2022**, *15*, 4131. [CrossRef] [PubMed]
24. Tao, Z.; Wang, Z.-B.; Yu, Q. Finite element modelling of concrete-filled steel stub columns under axial compression. *J. Constr. Steel Res.* **2013**, *89*, 121–131. [CrossRef]
25. Han, L.H. *Concrete-Filled Steel Tube Structures: Theory and Practice*; Science Press: Beijing, China, 2007.
26. Mander, J.B.; Priestley, M.J.N.; Park, R. Theoretical Stress-Strain Model for Confined Concrete. *J. Struct. Eng.* **1988**, *114*, 1804–1826. [CrossRef]
27. Teng, J.; Yu, T.; Wong, Y.; Dong, S. Hybrid FRP–concrete–steel tubular columns: Concept and behavior. *Constr. Build. Mater.* **2007**, *21*, 846–854. [CrossRef]
28. Pagoulatou, M.; Sheehan, T.; Dai, X.; Lam, D. Finite element analysis on the capacity of circular concrete-filled double-skin steel tubular (CFDST) stub columns. *Eng. Struct.* **2014**, *72*, 102–112. [CrossRef]
29. American Concrete Institute. *Building Code Requirements for Structural Concrete and Commentary, ACI 318-05*; American Concrete Institute: Farmington Hills, MI, USA, 2005.
30. Ji, J.; Yu, D.Y.; Jiang, L.Q.; Liu, Y.C.; Yang, M.M.; Song, H.Y.; Jiang, L. Research on axial compression bearing capacity of different-strength concrete-filled double steel tube short columns. *Build. Struct.* **2020**, *50*, 120–129. [CrossRef]
31. Luo, X.; Wei, J.G.; Han, J.P.; Han, B.C. Experimental study on compression performance of ultra-high- strength concrete (UHSC) filled high-strength steel tube stub columns subjected to eccentric load. *J. Build. Struct.* **2021**, *41*, 271–277. [CrossRef]
32. Guo, X.S. Behaviors of Axially Loaded and Eccentrically Loaded concrete-filled Elliptical Hollow Sections. Master's Thesis, Harbin Institute of Technology, Harbin, China, 2015.
33. *BS EN 1994-1-1: Eurocode 4*; Design of Composite Steel and Concrete Structures Part 1-1: General Rules and Rules for Buildings. British Standards Institution: London, UK, 2004.